Journal of Materials Chemistry A

ROYAL SOCIETY OF CHEMISTRY

PAPER

View Article Online
View Journal | View Issue

Cite this: J. Mater. Chem. A, 2024, 12, 12581

Investigation of the lithium plating triggering criterion in graphite electrodes†

Jiani Li,[a] Lubing Wang[b] and Jun Xu *[cd]

Lithium plating is considered an undesirable side reaction because it can induce capacity fading and pose safety concerns in Li-ion batteries. The timely detection of lithium plating onset is crucial for both mechanistic investigations and ensuring the safe and durable operation of batteries. In this study, discharging tests were conducted by varying the set capacity in graphite/Li cells to induce lithium plating on the graphite electrode. Based on a comprehensive analysis of the voltage curves and the morphological characterization of disassembled cells, the inflection point on the differential voltage curve during the discharging process was identified as the precise onset time of lithium plating. Electrochemical models were developed to further elucidate the mechanisms governing the onset of lithium plating. Compared with the model based on the potential criterion, the model employing the concentration criterion demonstrated enhanced precision in predicting lithium plating, particularly under high C rates. Based on the model with the concentration criterion, the discharging protocol was optimized parametrically to achieve high discharging efficiency and restrain lithium plating. This nuanced understanding contributes to determining the onset of lithium plating more accurately, thereby facilitating a more robust battery design and durable yet fast charging protocols.

Received 11th January 2024
Accepted 16th April 2024

DOI: 10.1039/d4ta00244j

rsc.li/materials-a

1. Introduction

Lithium-ion batteries (LIBs) have gained widespread recognition in consumer electronics[1,2] and electric transportation[3,4] owing to their outstanding attributes such as high energy density,[5] high power density,[6] prolonged lifecycle, and cost-effectiveness. During typical charging conditions, lithium ions intercalate into the layered structure of graphite in a series of stages, culminating in the formation of LiC_6 upon complete lithiation.[7] However, under specific conditions such as high charging rates (C rates),[8–10] overcharging,[11–13] and low temperatures,[14,15] lithium ions can undergo direct reduction to form metallic lithium on the graphite surface, a phenomenon known as "lithium plating". This unwanted side reaction may result in increased internal resistance, capacity fading,[16,17] Li dendrite formation,[18,19] and internal short circuits. Detecting the onset of lithium plating is imperative to determine the health and safety status of a running cell.

Various experimental methods have been employed to comprehensively understand lithium plating and detect its occurrence, including electrochemical techniques and physical characterization methods.[20] Leveraging the reaction of the plated Li metal with the electrolyte and the different electrochemical properties of the plated Li metal and intercalated carbon (Li_xC_6),[21] various electrochemical methods have been explored to detect lithium plating on graphite electrodes, such as the measurement of coulombic efficiency,[13] discharging/rest voltage curves[8,22–24] and the potential of graphite electrodes in cells in 2-electrode[25] and 3-electrode[26] setups. While these methods are nondestructive and convenient for engineering applications, they can only partially confirm the presence of plated lithium and do not detect the precise onset of lithium plating *in situ*.[20] Physical characterization methods such as optical microscopy,[10,27] scanning electron microscopy (SEM),[28] transmission electron microscopy (TEM),[29] nuclear magnetic resonance spectroscopy (NMR),[30] and *in situ* neutron diffraction,[17] offer direct detection of plated lithium metal but their widespread application is hindered by expensive equipment and implementation challenges. Consequently, there is a need for an economical, convenient, nondestructive, and accurate *in situ* method for detecting the onset of lithium plating.

Understanding the mechanism of lithium plating is imperative to determining its onset. Conventionally, it is considered that lithium plating becomes thermodynamically possible when the over-potential of the lithium plating reaction reaches a value smaller than 0 V *vs.* Li/Li^+ ($\eta_{pla} < 0$ V).[3,31,32] Elevated polarization resulting from high C rates[25] and low temperatures[33] contributes

[a]Department of Mechanical Engineering and Engineering Science, The University of North Carolina at Charlotte, Charlotte, NC 28223, USA
[b]Key Laboratory Impact & Safety Engineering, Ministry of Education, Ningbo University, Ningbo, Zhejiang 315211, China
[c]Department of Mechanical Engineering, University of Delaware, Newark, DE 19716, USA. E-mail: junxu@udel.edu; Fax: +1-302-831-0121; Tel: +1-302-831-0121
[d]Energy Sustainability and Mechanics Laboratory (ESMLab), University of Delaware, Newark, DE 19716, USA

† Electronic supplementary information (ESI) available. See DOI: https://doi.org/10.1039/d4ta00244j

to the reduction in graphite potential, thereby promoting the occurrence of lithium plating. However, although the potential criterion ($\eta_{pla} < 0$ V) is considered a necessary condition for lithium plating, it is insufficient, as demonstrated by several experiments.[26,34–37] Uhlmann *et al.*,[35] for instance, subjected graphite/Li cells to charging pulses at varying C rates after reaching a certain state of charge (SOC). Their results indicated that during charging pulses at 5C and 10C, lithium plating did not occur until the graphite potential fell significantly below 0 V. Gao *et al.*,[37] by utilizing *in situ* optical microscopy coupled with electrochemical measurements, observed that a single graphite particle could withstand a negative potential of −115 mV before any plated Li metal was observed during discharging at 0.6C. The above experiments were conducted on cells with a 2-electrode setup, which may affect the measurement accuracy of graphite potential due to polarization on the counter electrode. Based on this, Wandt *et al.*[26] performed forced lithium plating on cells with a 3-electrode setup. By employing *operando* electron paramagnetic resonance (EPR) spectroscopy, they observed that the onset of lithium plating happened at a negative graphite potential measured with a reference electrode setup. Besides, the electrolyte concentration gradient between the graphite electrode and reference electrode was less significant due to the low C rate of 0.1C, guaranteeing the measurement accuracy of graphite potential. It has been demonstrated that the potential criterion ($\eta_{pla} < 0$ V) alone is inadequate to determine lithium plating onset. Factors other than potential, such as concentration, may play vital roles in triggering lithium plating. Using *in situ* optical microscopy, some researchers[37–39] found that the lithium plating occurred exclusively on the fully lithiated parts of the graphite electrode, while the onset voltage was much below 0 V *versus* Li/Li^+.[37,38] Such observations illustrate that Li concentration in graphite is a more accurate indicator of lithium plating than graphite potential, and this has been rationalized by analyzing the energetics and kinetics of the lithium intercalation and lithium plating.[37] During the charging process, lithium intercalation is always more favored energetically and kinetically than lithium plating even when the potential criterion for lithium plating is satisfied ($\eta_{pla} < 0$ V). The tipping point occurs when the graphite surface is saturated with intercalated Li ions ($c_{s,surf} \geq c_{s,max}$). At this point, lithium intercalation is energetically equally favorable but kinetically less favorable than lithium plating due to the lack of sites for Li ions to intercalate and the drop in nucleation barrier for lithium plating. As a result, the intercalation reaction is restrained, and the applied current is redirected to lithium plating. Numerical models have been developed to predict the onset of lithium plating. While most researchers have traditionally adopted graphite potential as the primary indicator[13,32,40–42] that signifies lithium plating occurrence when the graphite potential falls below 0 V *vs.* Li/Li^+, it is emphasized that the potential criterion ($\eta_{pla} < 0$ V) is not universally applicable under all conditions, as mentioned previously. Therefore, the Li concentration in graphite has emerged as an equally critical parameter in modeling and predicting lithium plating onset.

In this study, our primary objective is the precise detection of the onset of lithium plating on graphite by exploring the underlying mechanisms through the synergistic integration of experiments and electrochemical modeling. To achieve this, discharging tests were conducted on graphite/Li cells by setting different capacities and intentionally inducing lithium plating on the graphite electrode. The onset of lithium plating was discerned by analyzing the indirect differential voltage curves and direct morphological characterization of the disassembled cells. Subsequently, an electrochemical model was formulated to provide a comprehensive understanding of the mechanism governing the onset of lithium plating. In addition, various models incorporating different lithium plating criteria, such as the potential criterion ($\eta_{pla} < 0$ V) and the concentration criterion ($c_{s,surf} \geq c_{s,max}$), were developed and systematically compared across different C rates. The modified criterion in our proposed model serves as a nuanced improvement, allowing for a more accurate depiction of the onset of lithium plating. Building upon the insights obtained from our models, we propose two optimal discharging protocols designed to enhance efficiency while mitigating the occurrence of lithium plating.

2. Experimental details

The electrochemical performance of the graphite electrode during overdischarge was assessed using CR2032 coin cells on an electrochemical workstation (Metrohm Autolab). The experimental cells were meticulously assembled in a glove box under an argon atmosphere using graphite as the working electrode and a Li plate as the counter electrode. The nominal capacity of the cells ($Q_n = 2.03$ mA h) was calculated from the material loading on the graphite electrode (ESI†). Before the formal tests, the experimental cells underwent a pre-cycling process at 0.1C, involving three consecutive from 0.005 V to 2 V. The charging capacity observed during the third cycle was the rated capacity. Subsequently, only cells exhibiting rated capacity in the 1.81–1.92 mA h range were selected for the subsequent formal tests. This stringent selection criterion was followed to ensure consistency and reliability of electrochemical performance evaluation during the overdischarge process of the graphite electrode.

In the formal experiments, the selected cells with similar rate capacities were discharged at 0.5C to different extents by setting different discharging capacities from 1 to 5 mA h. Subsequently, without any relaxation period, the cells were promptly charged at 0.5C until they reached a cut-off voltage of 2 V. Differential analyses[7,8,22] were then applied to the discharging and charging curves mentioned above by employing an indirect detection method to assess the occurrence of lithium plating during the discharging process. Furthermore, the morphology of the disassembled cells was characterized to detect lithium plating directly. Specifically, the cells were initially discharged at 0.5C to different extents and immediately disassembled within the confines of a glove box to prevent stripping of the plated Li metal and the potential reaction between Li metal and the air. Additionally, overdischarge tests of the cells were conducted at 0.1C and 0.2C to validate the numerical model. The equilibrium potential of the graphite electrode (Fig. S1(a)†) used in the model was derived from the discharging test conducted at 0.01C. This comprehensive experimental approach, encompassing indirect and direct detection methods and numerical

model validation, contributes to a robust understanding of lithium plating dynamics on the graphite electrode.

3. Numerical model

The electrochemical model applied in this work was developed based on the pseudo-two-dimensional (P2D) model,[14,43,44] which consists of a one-dimensional representation of the cell and a second dimension representing the spherical active material particles. The basic equations in the model consist of charge conservation equations that describe potential distribution in the solid and liquid phases, mass conservation equations to describe the Li concentration distribution in the solid and liquid phases, and electrochemical kinetic equations that describe the reaction rates of lithium intercalation and lithium plating. In most cases,[12,13,16,31,32] the potential of graphite is commonly used as the indicator of lithium plating. Lithium plating starts when the graphite potential drops below 0 V *vs.* Li/Li^+. However, according to the assumption of solid diffusion limitation in graphite,[37,45] lithium plating is triggered when the inserted Li ions saturate the graphite surface due to slow solid diffusion compared with intercalation. Accordingly, the criterion of Li concentration needs to be considered in some cases. In this work, a model with the concentration criterion is established to predict the onset of lithium plating and analyze the underlying mechanism.

3.1. Charge conservation equations

In the battery, the solid-phase potential distribution is governed by Ohm's law:[43,46]

$$\nabla \times (\sigma_s^{eff} \nabla \varphi_s) = j_{total} \quad (1)$$

where σ_s^{eff} is the effective electrical conductivity of the solid phase, φ_s denotes the potential of the solid phase, and j_{total} is defined as the total volumetric current density of all electrochemical reactions. The boundary conditions at the current collector/graphite interface and graphite/separator interface are listed below, where i_{app} represents the applied current density.

$$-\sigma_s^{eff} \nabla \varphi_s \big|_{cc/gr}^{interface} = -i_{app} \quad (2)$$

$$-\sigma_s^{eff} \nabla \varphi_s \big|_{gr/sep}^{interface} = 0 \quad (3)$$

The governing equation of the liquid phase potential distribution and the corresponding boundary conditions at the current collector/graphite interface and graphite/separator interface are as follows:

$$-\nabla \times \left(\sigma_l^{eff} \nabla \varphi_l\right) + \frac{2RT(1-t^+)}{F}\left(1 + \frac{d \ln f}{d \ln c_l}\right) \nabla \times \left(\sigma_l^{eff} \nabla \ln c_l\right) = j_{total} \quad (4)$$

$$-\sigma_l^{eff} \nabla \varphi_l \big|_{cc/gr}^{interface} = 0 \quad (5)$$

$$-\sigma_l^{eff} \nabla \varphi_l \big|_{gr/sep}^{interface} = -i_{app} \quad (6)$$

where σ_l^{eff} is the effective electrical conductivity of the liquid phase, and φ_s is the potential of the liquid phase. R, T and F are the gas constant, temperature, and Faraday constant, respectively. t^+ represents the number of Li^+ transported, f is the activity coefficient, and c_l denotes the Li^+ concentration in the liquid phase.

3.2. Mass conservation equations

The distribution of Li concentration inside the solid active material particles follows Fick's law[47] (eqn (7)). c_s denotes the Li concentration in the solid phase, D_s represents the solid phase diffusion coefficient (Fig. S2†), and r is the radius of the particle. The boundary condition at the particle center ($r = 0$) (eqn (8)) indicates that no Li source exists at the center of the particle. At the particle surface ($r = R_s$), the Li flux is determined by the local current density of lithium intercalation (j_{int}). Here a_s represents the specific surface area of the particle.

$$\frac{\partial c_s}{\partial t} = D_s\left(\frac{2}{r}\frac{\partial c_s}{\partial r} + \frac{\partial^2 c_s}{\partial r^2}\right) \quad (7)$$

$$\left.\frac{\partial c_s}{\partial r}\right|_{r=0} = 0 \quad (8)$$

$$-D_s \left.\frac{\partial c_s}{\partial r}\right|_{r=R_s} = \frac{j_{int}}{a_s F} \quad (9)$$

Li^+ distribution in the liquid phase is directed by the Nernst–Plank equation (eqn (10)).[48] The related boundary condition at the current collector/graphite interface is expressed as eqn (11).

$$\varepsilon_l \frac{\partial c_l}{\partial t} = -\nabla \times (J_l) + \frac{j_{total}}{F} \quad (10)$$

$$-\nabla c_l \big|_{cc/gr}^{interface} = 0 \quad (11)$$

where c_l and ε_l represent the Li^+ concentration and volume fraction of the liquid phase, respectively. J_l is defined as the Li^+ flux density in the liquid phase, which is related to c_l and i_l (liquid phase current density), as follows:

$$J_l = -D_l^{eff} \nabla c_l + \frac{t^+}{F} i_l \quad (12)$$

$$i_l = -\sigma_l^{eff} \nabla \varphi_l + \frac{2RT(1-t^+)}{F}\left(1 + \frac{d \ln f}{d \ln c_l}\right)\left(\sigma_l^{eff} \nabla \ln c_l\right) \quad (13)$$

3.3. Electrochemical kinetic equations

During the overdischarging process of the graphite/Li cell, lithium intercalation is the main electrochemical reaction at the surface of the graphite particles, while lithium plating is regarded as a side reaction that takes place when the required criterion is satisfied. Accordingly, the total volumetric current density j_{total} is the sum of the current densities of lithium plating j_{pla} and lithium intercalation j_{int}.

$$j_{\text{total}} = j_{\text{pla}} + j_{\text{int}} \quad (14)$$

As mentioned above, j_{total} is used in the charge conservation eqn (1) and (4) and the mass conservation eqn (10) as the reaction source. However, only j_{int} is applied as the reaction source in eqn (9) since lithium present inside the particle comes entirely from lithium intercalation at the particle surface, irrelevant to lithium plating.

The volumetric current density of lithium plating j_{pla} is expressed by the Butler–Volmer equation presented as eqn (15). Unlike the widely used models, which adopt the overpotential of lithium plating as the indicator of lithium plating ($\eta_{\text{pla}} < 0$ V),[12,13,16,31,32] the Li concentration criterion is applied in the current model. Specifically, the expression of the exchange current density of lithium plating $i_{0,\text{pla}}$ (eqn (16)) indicates that lithium plating is induced when the Li concentration at the particle surface $c_{\text{s,surf}}$ exceeds the maximum value $c_{\text{s,max}}$.

$$j_{\text{pla}} = a_{\text{s}} i_{0,\text{pla}} \left[\exp\left(\frac{\alpha_{\text{a,pla}} F \eta_{\text{pla}}}{RT} \right) - \exp\left(-\frac{\alpha_{\text{c,pla}} F \eta_{\text{pla}}}{RT} \right) \right] \quad (15)$$

$$i_{0,\text{pla}} = F k_{\text{pla}} c_{\text{l}} (c_{\text{s,surf}} \geq c_{\text{s,max}}) \quad (16)$$

$$\eta_{\text{pla}} = \varphi_{\text{s}} - \varphi_{\text{l}} - E_{\text{eq,pla}} - \frac{j_{\text{total}}}{a_{\text{s}}} R_{\text{film}} \quad (17)$$

$\alpha_{\text{c,pla}}$ and $\alpha_{\text{a,pla}}$ are the charge transfer coefficients of the cathode and anode, respectively. k_{pla} represents the reaction rate constant for lithium plating. η_{pla} is the overpotential of lithium plating, and $E_{\text{eq,pla}}$ is the equilibrium potential of lithium plating, which equals 0 V *vs.* Li/Li$^+$. R_{film} represents the resistance of the surface film.

The volumetric current density of lithium intercalation j_{int} is also expressed by the Butler–Volmer equation.[31]

$$j_{\text{int}} = a_{\text{s}} i_{0,\text{int}} \left[\exp\left(\frac{\alpha_{\text{a,int}} F \eta_{\text{int}}}{RT} \right) - \exp\left(-\frac{\alpha_{\text{c,int}} F \eta_{\text{int}}}{RT} \right) \right] \quad (18)$$

where $i_{0,\text{int}}$ represents the exchange current density of lithium intercalation, which is expressed as

$$i_{0,\text{int}} = F k_{\text{int}} {c_{\text{s,surf}}}^{\alpha_{\text{c,int}}} {\Delta c_{\text{s}}}^{\alpha_{\text{a,int}}} \left(\frac{c_{\text{l}}}{c_{\text{l,ref}}} \right)^{\alpha_{\text{a,int}}} \quad (19)$$

$$\Delta c_{\text{s}} = \min\{\max[(c_{\text{s,max}} - c_{\text{s,surf}}), c_{\text{s1}}], c_{\text{s2}} - c_{\text{s,surf}}\} \quad (20)$$

η_{int} is the overpotential of lithium intercalation, which is calculated as

$$\eta_{\text{int}} = \varphi_{\text{s}} - \varphi_{\text{l}} - E_{\text{eq,int}} - \frac{j_{\text{total}}}{a_{\text{s}}} R_{\text{film}} \quad (21)$$

The general expression of Δc_{s} in a traditional P2D model is $\Delta c_{\text{s}} = c_{\text{s,max}} - c_{\text{s,surf}}$,[13,32] which will lead to non-convergence in models with the concentration criterion (ESI†). To avoid computational conflict and simulate the transition from lithium intercalation to lithium plating during the discharging progress, Δc_{s} was modified as the function of $c_{\text{s,surf}}$ (eqn (20)), as depicted in Fig. S2.† c_{s1} and c_{s2} are the parameters that define Δc_{s} and are adjusted by the calibration of the experimental and simulated voltages. Besides, k_{int} is the reaction rate constant, and $c_{\text{l,ref}}$ represents the reference Li$^+$ concentration in the liquid phase. $\alpha_{\text{c,int}}$ and $\alpha_{\text{a,int}}$ are the charge transfer coefficients of the cathode and anode, respectively. $E_{\text{eq,int}}$ is the equilibrium potential of lithium intercalation on graphite (Fig. S1(a)†).

Based on mass conservation, the thickness of the plated Li metal layer δ_{pla} can be expressed as:

$$\frac{\partial \delta_{\text{pla}}}{\partial t} = -\frac{j_{\text{pla}} M_{\text{pla}}}{a_{\text{s}} \rho_{\text{pla}} F} \quad (22)$$

where M_{pla} and ρ_{pla} represent the molar weight and density of the plated Li metal, respectively. Then, the resistance of the Li metal film can be determined by the thickness δ_{pla} and conductivity σ_{film} of the plated Li metal.

$$R_{\text{film}} = \frac{\delta_{\text{pla}}}{\sigma_{\text{film}}} \quad (23)$$

Besides, the pores in the graphite electrode are occupied by plated Li metal. As a result, the porosity of graphite can be written as:

$$\varepsilon_{\text{l}} = \varepsilon_{\text{l,0}} - a_{\text{s}} \delta_{\text{pla}} \quad (24)$$

The model was established and presented in COMSOL Multiphysics. The electrochemical parameters applied in the model are listed in Table S2.†

4. Results and discussion

4.1. Detection of the onset of lithium plating *via* experiments

To induce lithium plating on the graphite electrode and detect the onset of lithium plating, overdischarge tests were conducted on graphite/Li cells with 1.0 M $LiPF_6$/EC + PC + EDC (1 : 1 : 1) as the electrolyte. Four cells denoted as A1–A4 were discharged at 0.5C to different extents by setting different discharging capacities (A1: 4.53 mA h, A2: 2.14 mA h, A3: 1.70 mA h, and A4: 1.38 mA h), and then immediately charged at 0.5C to 2 V with no relaxation. The U–Q and dU/dQ–Q curves of the discharging process (Fig. 1(a)) show the reliable repeatability of cell performance. The curves obtained during the subsequent charging process (Fig. 1(b)) were further analyzed to help determine the onset of Lithium plating. Lithium stripping plateaus were observed in the starting stage of the U–Q curves of cells A1 and A2. These stripping plateaus are attributed to the preferential stripping of plated Li metal due to its lower standard potential than lithium intercalated inside graphite.[21] Besides, the peaks in the dU/dQ–Q curves of cells A1 and A2 correspond with the transition from lithium stripping to lithium deintercalation, which indicates that the capacity at the dU/dQ peak can be regarded as the amount of reversible Li metal. The lithium stripping plateau and peak indicate that lithium stripping occurs during the initial charging process in cells A1 and A2. Furthermore, they demonstrate that lithium plating occurs

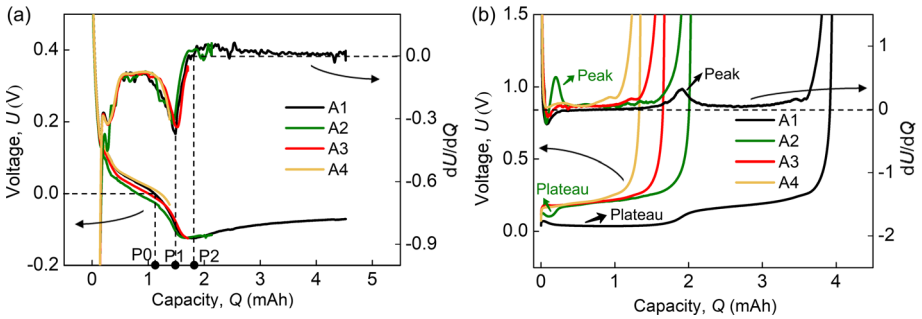

Fig. 1 The U–Q and dU/dQ–Q curves cells A1 to A4 during (a) discharging tests to different capacities and (b) charging tests.

during the overdischarging process in A1 and A2. Cells A3 and A4 had no obvious Li stripping plateau or peak during the charging process (Fig. 1(b)). There are two possible explanations for this phenomenon: (i) lithium stripping does not occur during charging; (ii) lithium stripping occurs, but the amount of plated Li metal is too small to be detected. As a result, it is challenging to determine if lithium plating occurred in cells A3 and A4 during the discharging process.

The results confirm that lithium plating occurs in cells A1 and A2 during the discharging process. Based on this, three possible locations for lithium plating onset defined as P0, P1, and P2 were identified according to the characteristics of the U–Q and dU/dQ–Q curves obtained during discharging (Fig. 1(a)). P0 was defined at $U = 0$ V since most researchers[12,13,31,32] believe that lithium plating occurs when the graphite voltage drops below 0 V (based on potential criterion). P1 was defined at the valley of dU/dQ–Q. In comparison with the normal discharge test at 0.01C (Fig. S1(b)†), the dU/dQ–Q curve of the over-discharge test at 0.5C (Fig. 1(a)) presented an additional valley at around 1.63 mA h, which may result from the occurrence of lithium plating. Further, P2 was defined at dU/dQ = 0, representing the onset of the final plateau stage of the U–Q curve. Generally, the plateaus of the U–Q curve represent the coexisting phase regions since the chemical potential of Li in coexisting phases is equal.[49] Accordingly, the plateau after P2 represents the coexisting phase region of LiC_6 and Li metal.

To further determine the onset of lithium plating, the morphologies of the disassembled cells with varying discharging capacities were systematically characterized (Fig. 2). Cells B1 and B2 were discharged to capacities exceeding P2 (Fig. 2(a)) and promptly disassembled within the glove box. Evident silver Li metal deposits were observed on the graphite surface of both B1 and B2 (Fig. 2(b)). Cell B3, which was discharged to a capacity surpassing P1 but lower than P2 (Fig. 2(a)), exhibited a modest amount of Li metal on its graphite surface (Fig. 2(b)). In contrast, cell B4, which was discharged to a capacity below P1, displayed no discernible plated Li metal on the disassembled graphite electrode. Consequently, it can be inferred that the onset of lithium plating happens at a capacity value between those of B3 and B4, close to or precisely at P1. This characterization allows for the precise identification of the lithium plating onset point in the specific discharge capacity range defined by cells B3 and B4. Besides, the graphite voltage range between B3 and B4 (−0.076 to −0.021 V) indicates that lithium plating occurs at a negative graphite voltage, which is not explained by the traditional potential criterion ($\eta_{pla} < 0$ V).[3,31,32] As described in some reports,[37,50,51] Li concentration in graphite is considered as the indicator of lithium plating instead of graphite voltage. In this case, lithium plating may be induced since Li concentration on the graphite particle surface reaches the saturation level.

4.2. Detection of the onset of lithium plating *via* simulations

The above experiments provide a relatively narrow range for lithium plating onset, yet the precise location of lithium plating onset and the underlying mechanism were confirmed and interpreted by simulation. Considering that the potential criterion ($\eta_{pla} < 0$ V) is not suitable to elucidate the occurrence of lithium plating in this case, a model was established using the concentration criterion for lithium plating ($c_{s,surf} \geq c_{s,max}$). Fig. 3(a–c) show the model predictions, in which the dashed lines denote the experimental results, while the simulated results are shown by solid lines. The simulated U–t and dU/dt–t curves of the overdischarging cases at 0.1C, 0.2C, and 0.5C fitted the experimental results well, validating the accuracy of the model. Besides, according to the rate of plated Li metal concentration variation dc_{li}/dt, the turning point of the simulated dc_{li}/dt curve can be determined as the onset of lithium plating and is denoted as t_M. When lithium plating occurs at t_M, valley points appear on the simulated dU/dt–t curves in all cases, indicating that this valley point P1 arises due to the occurrence of lithium plating. Based on this, the valley points on the experimental dU/dt–t curves can be determined as the experimental onset points of lithium plating t_E. Therefore, this model with the concentration criterion can precisely predict the actual lithium plating onset point ($t_E \approx t_M$) at various C rates.

Further analysis was conducted to interpret the relationship between lithium plating occurrence and the valley point on the dU/dt–t curve (Fig. 3(d)). When lithium plating occurs, the current density of plating i_{pla} starts to increase from 0, while the current density of intercalation i_{int} starts to decrease. As

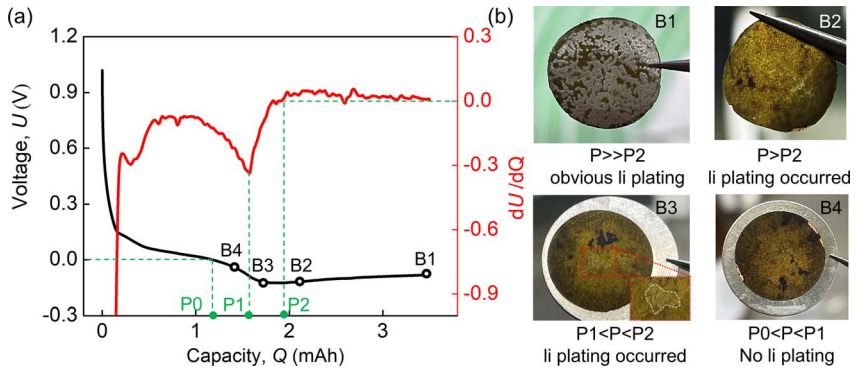

Fig. 2 (a) Curves of cells B1–B4 discharged at 0.5C to different capacities. (b) Morphology of the graphite electrodes disassembled from cells B1–B4.

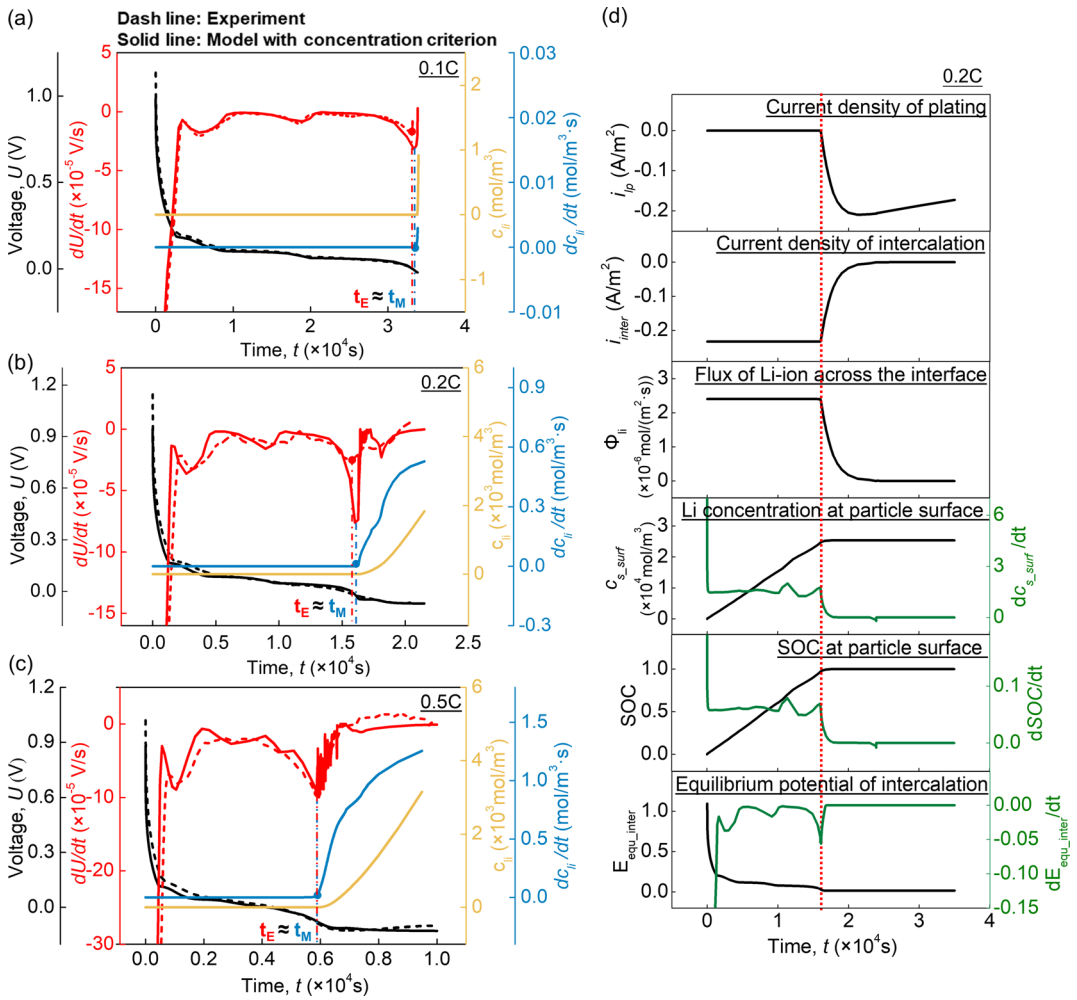

Fig. 3 Comparison of results obtained from the model with the concentration criterion and the overdischarging tests at (a) 0.1C, (b) 0.2C, and (c) 0.5C. (d) The mechanism underlying the appearance of the valley point in the dU/dt–t curve.

a result, the flux of Li ions across the particle surface Φ_{li}, which is determined by i_{int}, starts to decrease. With the decrement of Φ_{li}, the Li concentration and SOC at the particle surface keep increasing, but the corresponding variation rates (dc_{s_surf}/dt, $dSOC/dt$) begin to decrease. Since the equilibrium potential of intercalation E_{equ_int} is the function of SOC, the decrease in

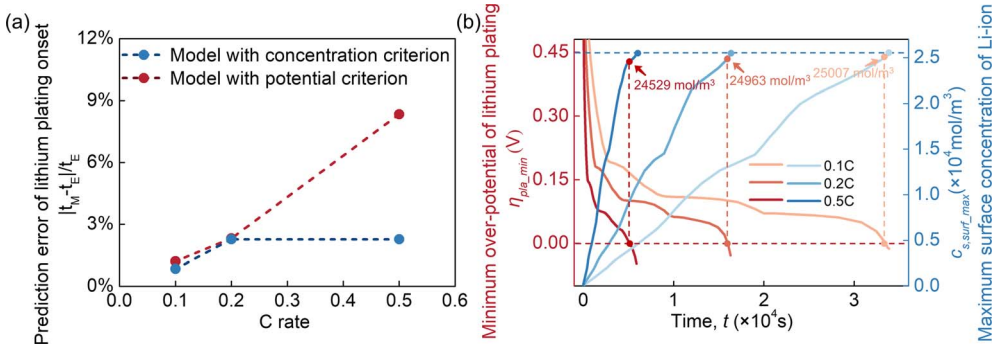

Fig. 4 (a) Comparison of results predicted using the models with the concentration criterion and the potential criterion at different C rates. (b) The evolution of the minimum overpotential of lithium plating η_{pla_min} and the maximum surface concentration of Li ions $c_{s,surf\_max}$ in the graphite electrodes at different C rates.

dSOC/dt leads to a decrease in dE_{equ_int}/dt, which finally causes the valley on the dU/dt–t curve.

As described above, the model with the concentration criterion can predict the onset of lithium plating precisely. To further demonstrate the superiority of the concentration criterion in lithium plating onset prediction, the simulated results obtained using the models based on the concentration criterion ($c_{s,surf} \geq c_{s,max}$) and the potential criterion ($\eta_{pla} < 0$ V) were compared. The governing equations and results of the model based on the potential criterion ($\eta_{pla} < 0$ V) (Fig. S3†) are given in detail as ESI.† In order to quantify the accuracy of the model in lithium plating onset prediction, the prediction error of the lithium plating onset time ε is defined as the ratio of the interval between the time of simulated and experimental lithium plating onset ($|t_M - t_E|$) to the experimental lithium plating onset time (t_E). As shown in Fig. 4(a), for the model with the potential criterion, the error in predicted lithium plating onset ε generally increased from 1.21% to 8.34% as the C rate varied from 0.1C to 0.5C. In comparison, ε of the model involving the concentration criterion increased initially from 0.84% to 2.27% as the C rate was changed from 0.1C to 0.2C but remained at this level while the C rate was increased from 0.2C to 0.5C. These results demonstrate that the concentration criterion is more suitable to predict the actual lithium plating onset time under a high C rate than the potential criterion. The adoption of the concentration criterion can keep the lithium plating onset prediction error at a relatively low level for all C rates, indicating that experimental lithium plating is more likely to be induced by the saturated Li concentration on the graphite particle surface rather than the negative overpotential of lithium plating.

Furthermore, the evolution of the minimum overpotential of lithium plating η_{pla_min} in the graphite electrode at different C rates and the maximum surface concentration of Li ions $c_{s,surf\_max}$ among these graphite electrodes were extracted and analyzed, as shown in Fig. 4(b) η_{pla_min} continued to decrease as time increased, and the potential criterion was triggered when η_{pla_min} reached 0 V (red circle). $c_{s,surf\_max}$ continued to increase with time, and the concentration criterion was triggered when $c_{s,surf\_max}$ reached c_{s_max} (blue circle). It was observed that the potential criterion was triggered earlier than the concentration criterion in all cases. As the C rate increased, the difference between the triggering times of the potential criterion and the concentration criterion became larger since $c_{s,surf\_max}$ at the potential criterion triggering time (red circle) decreased. As a result, the lithium plating onset time predicted by the model with the potential criterion was earlier than the actual lithium plating onset at a high C rate of 0.5C (Fig. S3(c)†).

4.3. Optimal discharging protocol

By applying the concentration criterion for lithium plating, the model can precisely predict the lithium plating onset under various C rates. Based on this, the discharging protocol was optimized to restrain lithium plating and enhance the discharging efficiency. First, two typical protocols CC(0.5C)_CV and CC(0.5C)_CC(0.4C) are proposed (Fig. 5(a) and (b)). In CC(0.5C)_CV, the cell is discharged at a constant current of 0.5C (grey part) until the concentration criterion of lithium plating is triggered ($c_{s,surf} = c_{s,max}$); then the cell is discharged at a constant voltage to a certain SOC (green part). The simulated result of the current density of lithium plating i_{pla} shows that lithium plating occurs at the starting point of the CV process since $c_{s,surf}$ continues to increase and remains larger than $c_{s,max}$ during the CV process. The traditional CC_CV protocol cannot restrain lithium plating. In CC(0.5C)_CC(0.4C), as shown in Fig. 5(b), the cell is discharged at 0.5C (grey part) until $c_{s,surf} = c_{s,max}$; then it is discharged at 0.4C to a certain SOC (green part). During the CC(0.4C) process, $c_{s,surf}$ first decreases from $c_{s,max}$ and then increases to exceed $c_{s,max}$. As a result, the onset of lithium plating is postponed in CC(0.5C)_CC(0.4C) compared with CC(0.5C)_CV.

Furthermore, different C rates denoted as nC (n = 0.1, 0.2, 0.3, and 0.4) were adopted for the second CC process, and the effects of C rate (nC) were analyzed, as presented in Fig. 5(c–f). As the C rate decreased from 0.4C to 0.1C, the voltage recovery at the starting point of the CC(nC) process increased from 0.02 V to 0.11 V. Besides, while the C rate decreased from 0.4C to 0.2C,

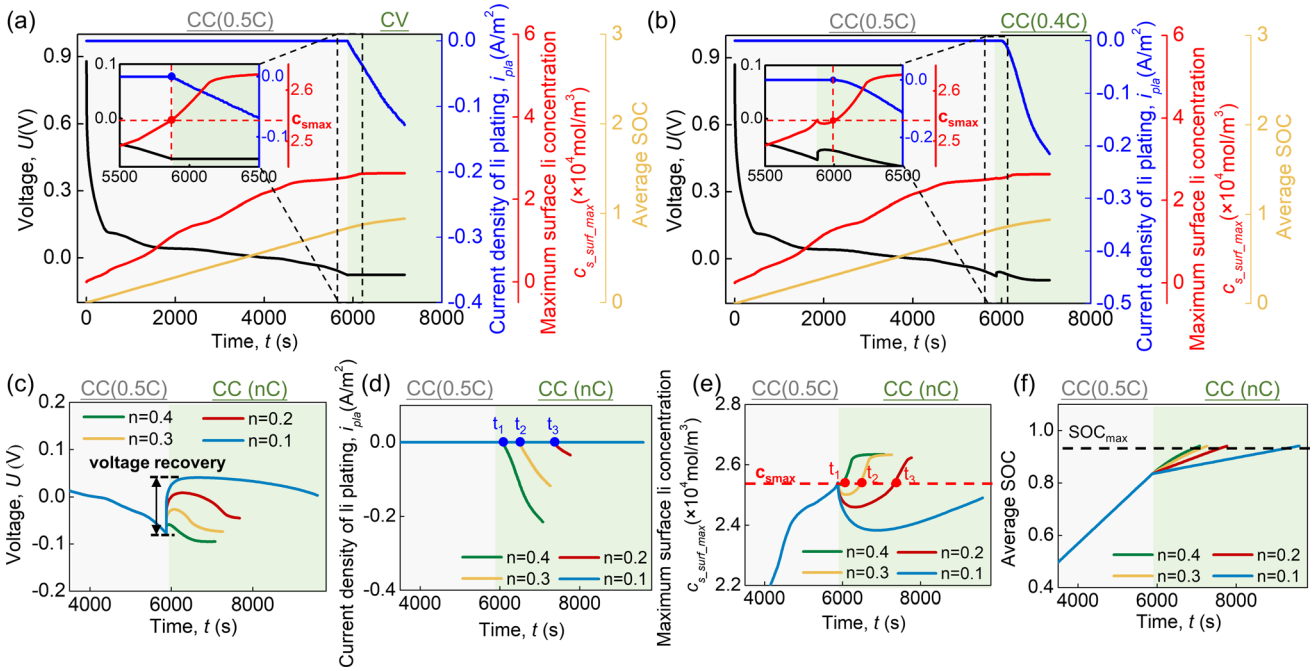

Fig. 5 Results of the optimized (a) CC(0.5C)_CV and (b) CC(0.5C)_CC(0.4C) protocols based on the prediction model based on the concentration criterion. (c) Voltage and (d) current density of lithium plating, (e) the maximum surface Li concentration, and (f) average SOC of the CC(0.5C)_CC(*n*C) protocols at different *n* values.

Table 1 Multi-CC discharging protocols

Name	*C*-rate of each CC step	Δ*C* rate
Mode 1	0.5C_0.1C	0.4C
Mode 2	0.5C_0.3C_0.1C	0.2C
Mode 3	0.5C_0.4C_0.3C_0.2C_0.1C	0.1C
Mode 4	0.5C_0.45C_0.4C_0.35C_0.3C_0.25C_0.2C_0.15C_0.1C	0.05C

the onset of lithium plating was postponed from t_1 (6027 s) to t_3 (7340 s) (Fig. 5(d)) since that the triggering time of the concentration criterion $c_{s,surf} \geq c_{s,max}$ is postponed from t_1 (6027 s) to t_3 (7340 s) (Fig. 5(e)). It should be noted that lithium plating would not occur in the CC(0.5C)_CC(0.1C) case since the concentration criterion is not triggered during the whole discharging process. Although the decrease in the C rate in the second CC process contributes to the delay in lithium plating, the discharging efficiency also becomes poorer since it takes more discharging time to reach the set discharging SOC. Besides, when lithium plating occurs respectively at t_1 (6027 s), t_2 (6400 s) and t_3 (7340 s) for $n = 0.4$, 0.3 and 0.2 (Fig. 5(d)), valley points appear on the dU/dt–t curves (Fig. 5(c)). The specific valley points on dU/dt–t curves can be recognized as the indicator of concentration saturation at the graphite particle surface and lithium plating occurrence. Accordingly, the lithium plating onset point can be detected *in situ* by monitoring the dU/dt–t data, which is simple and suitable for engineering applications.

As mentioned above, lithium plating is not induced when the cell is discharged according to CC(0.5C)_CC(0.1C). Based on this protocol and the model involving the concentration criterion, four multi-CC discharging protocols (Table 1, modes 1–4) are proposed by inserting CC steps between CC(0.5C) and CC(0.1C). The Δ*C* rate is defined as the difference in C rates between the adjacent CC steps. The multi-CC discharging protocols are based on the concentration criteria of lithium plating. Specifically, the transition between two adjacent CC steps is induced when the concentration criterion is triggered ($c_{s,surf} = c_{s,max}$). No lithium plating occurs in these four modes (Fig. 6(b)) since $c_{s,surf}$ remains lower than or equal to $c_{s,max}$ during the whole discharging process (Fig. 6(c)). Besides, as the Δ*C* rate decreases from 0.4C (mode 1) to 0.05C (mode 4), the discharging time to reach the set discharging SOC becomes shorter (Fig. 6(d)). This indicates that decreasing the Δ*C* rate in the multi-CC protocol can enhance the discharging efficiency of the cell with no lithium plating.

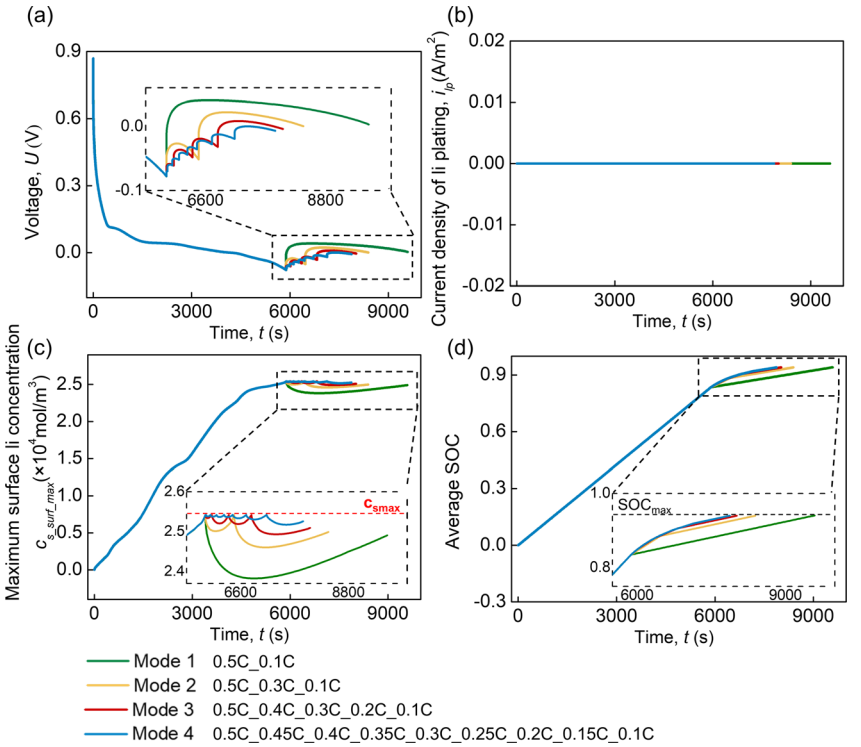

Fig. 6 (a) Voltage and (b) current density of lithium plating, (c) the maximum surface Li concentration, and (d) average SOC in the multi-CC discharging protocols with different ΔC rates.

5. Conclusions

Detecting the initiation of lithium plating on graphite electrodes holds paramount importance in ensuring the safety of batteries. In this study, we conducted a comprehensive experimental investigation to precisely determine the onset of lithium plating on graphite. Additionally, we developed electrochemical models by employing different lithium plating criteria, specifically the potential and concentration criteria, to elucidate the mechanisms governing the initiation of lithium plating. Using the modified model, a parametric study was undertaken to derive an optimized discharging protocol that not only exhibits high discharging efficiency but also mitigates the occurrence of lithium plating. The key findings and conclusions drawn from this research can be summarized as follows:

(1) We introduced and validated a novel method for the *in situ* detection of the onset of lithium plating based on the distinctive characteristics of the dU/dt–t curve. The valley point, denoted as P1, in the dU/dt–t curve of the discharging process was established as a precise indicator of the initiation of lithium plating.

(2) Electrochemical models incorporating distinct lithium plating criteria were formulated and examined. Comparative analysis revealed that the model incorporating a concentration criterion demonstrated superior suitability in predicting the onset of lithium plating, particularly under elevated C rates, in contrast to the model that relied on a potential criterion.

(3) In the context of multi-CC (constant current) protocols, our investigation determined that the reduction in ΔC rate between adjacent CC steps contributes to an enhanced discharging efficiency, while concurrently mitigating the occurrence of lithium plating. This finding underscores the significance of protocol design in achieving optimal battery performance with minimal risk of lithium plating.

These findings contribute to advancing the understanding of lithium plating phenomena and offer practical implications for the design and operation of lithium-ion batteries to enhance both safety and efficiency.

Data availability

The datasets used in this study are available from the corresponding author upon request.

Conflicts of interest

The authors declare no competing interests for this work.

Acknowledgements

L. W. appreciates the financial support from the National Science Foundation of China (12102212, 11872099).

References

1 J. Zhang, Y. Wang, B. Jiang, H. He, S. Huang, C. Wang, Y. Zhang, X. Han, D. Guo, G. He and M. Ouyang, *Nat. Commun.*, 2023, **14**, 5940.
2 S. Li, J. Niu, Y. C. Zhao, K. P. So, C. Wang, C. A. Wang and J. Li, *Nat. Commun.*, 2023, **14**, 5664.
3 T. Waldmann, B.-I. Hogg and M. Wohlfahrt-Mehrens, *J. Power Sources*, 2018, **384**, 107–124.
4 B. Liu, X. Duan, C. Yuan, L. Wang, J. Li, D. P. Finegan, B. Feng and J. Xu, *J. Mater. Chem. A*, 2021, **9**, 7102–7113.
5 X. Gao, W. Lu and J. Xu, *Nano Energy*, 2021, **81**, 105591.
6 W. Wu, X. Xiao and X. Huang, *Electrochim. Acta*, 2012, **83**, 227–240.
7 S. Weng, S. Wu, Z. Liu, G. Yang, X. Liu, X. Zhang, C. Zhang, Q. Liu, Y. Huang and Y. Li, *Carbon Energy*, 2023, **5**, 10.
8 Y. Chen, L. Torres-Castro, K.-H. Chen, D. Penley, J. Lamb, M. Karulkar and N. P. Dasgupta, *J. Power Sources*, 2022, **539**, 231601.
9 K. S. N. Vikrant and S. Allu, *J. Electrochem. Soc.*, 2021, **168**, 020536.
10 Y. Chen, K.-H. Chen, A. J. Sanchez, E. Kazyak, V. Goel, Y. Gorlin, J. Christensen, K. Thornton and N. P. Dasgupta, *J. Mater. Chem. A*, 2021, **9**, 23522–23536.
11 D. Ren, X. Feng, L. Lu, X. He and M. Ouyang, *Appl. Energy*, 2019, **250**, 323–332.
12 W. Mei, L. Zhang, J. Sun and Q. Wang, *Energy Storage Mater.*, 2020, **32**, 91–104.
13 W. Mei, L. Jiang, C. Liang, J. Sun and Q. Wang, *Energy Storage Mater.*, 2021, **41**, 209–221.
14 T. Sun, T. Shen, Y. Zheng, D. Ren, W. Zhu, J. Li, Y. Wang, K. Kuang, X. Rui, S. Wang, L. Wang, X. Han, L. Lu and M. Ouyang, *Electrochim. Acta*, 2022, **425**, 140701.
15 M. Storch, J. P. Fath, J. Sieg, D. Vrankovic, C. Krupp, B. Spier and R. Riedel, *J. Energy Storage*, 2021, **41**, 102887.
16 X.-G. Yang, Y. Leng, G. Zhang, S. Ge and C.-Y. Wang, *J. Power Sources*, 2017, **360**, 28–40.
17 N. Paul, J. Wandt, S. Seidlmayer, S. Schebesta, M. J. Mühlbauer, O. Dolotko, H. A. Gasteiger and R. Gilles, *J. Power Sources*, 2017, **345**, 85–96.
18 C. Yuan, X. Gao, Y. Jia, W. Zhang, Q. Wu and J. Xu, *Nano Energy*, 2021, **86**, 106057.
19 X. Yang, X. Gao, C. Zhao, Q. Sun, Y. Zhao, K. Adair, J. Luo, X. Lin, J. Liang, H. Huang, L. Zhang, S. Lu, R. Li and X. Sun, *Energy Storage Mater.*, 2020, **27**, 198–204.
20 P. P. Paul, E. J. McShane, A. M. Colclasure, N. Balsara, D. E. Brown, C. Cao, B.-R. Chen, P. R. Chinnam, Y. Cui, E. J. Dufek, D. P. Finegan, S. Gillard, W. Huang, Z. M. Konz, R. Kostecki, F. Liu, S. Lubner, R. Prasher, M. B. Preefer, J. Qian, M.-T. F. Rodrigues, M. Schnabel, S.-B. Son, V. Srinivasan, H.-G. Steinrück, T. R. Tanim, M. F. Toney, W. Tong, F. Usseglio-Viretta, J. Wan, M. Yusuf, B. D. McCloskey and J. Nelson Weker, *Adv. Energy Mater.*, 2021, **11**, 2100372.
21 Q. Liu, C. Du, B. Shen, P. Zuo, X. Cheng, Y. Ma, G. Yin and Y. Gao, *RSC Adv.*, 2016, **6**, 88683.
22 M. Koseoglou, E. Tsioumas, D. Ferentinou, I. Panagiotidis, N. Jabbour, D. Papagiannis and C. Mademlis, *J. Energy Storage*, 2022, **54**, 105345.
23 A. Adam, E. Knobbe, J. Wandt and A. Kwade, *J. Power Sources*, 2021, **495**, 229794.
24 X.-G. Yang, S. Ge, T. Liu, Y. Leng and C.-Y. Wang, *J. Power Sources*, 2018, **395**, 251–261.
25 M.-T. F. Rodrigues, K. Kalaga, S. E. Trask, D. W. Dees, I. A. Shkrob and D. P. Abraham, *J. Electrochem. Soc.*, 2019, **166**, A996–A1003.
26 J. Wandt, P. Jakes, J. Granwehr, R.-A. Eichel and H. A. Gasteiger, *Mater. Today*, 2018, **21**, 231–240.
27 C. Fear, T. Adhikary, R. Carter, A. N. Mistry, C. T. Love and P. P. Mukherjee, *ACS Appl. Mater. Interfaces*, 2020, **12**, 30438–30448.
28 S. P. Rangarajan, Y. Barsukov and P. P. Mukherjee, *J. Mater. Chem. A*, 2019, **7**, 20683–20695.
29 H. Park, Y. Jeon, W. J. Chung, Y. Bae, J. Kim, H. Baek and J. Park, *ACS Energy Lett.*, 2023, **8**, 715–721.
30 H. Ge, T. Aoki, N. Ikeda, S. Suga, T. Isobe, Z. Li, Y. Tabuchi and J. Zhang, *J. Electrochem. Soc.*, 2017, **164**, A1050–A1060.
31 P. Arora, M. Doyle and R. E. White, *J. Electrochem. Soc.*, 1999, **146**, 3543–3553.
32 C. von Lüders, J. Keil, M. Webersberger and A. Jossen, *J. Power Sources*, 2019, **414**, 41–47.
33 M. Angeles Cabañero, J. Altmann, L. Gold, N. Boaretto, J. Müller, S. Hein, J. Zausch, J. Kallo and A. Latz, *Energy*, 2019, **171**, 1217–1228.
34 I. A. Shkrob, M.-T. F. Rodrigues, D. W. Dees and D. P. Abraham, *J. Electrochem. Soc.*, 2019, **166**, A3305–A3313.
35 C. Uhlmann, J. Illig, M. Ender, R. Schuster and E. Ivers-Tiffée, *J. Power Sources*, 2015, **279**, 428–438.
36 M. W. Verbrugge and B. J. Koch, *J. Electroanal. Chem.*, 1997, **436**, 1–7.
37 T. Gao, Y. Han, D. Fraggedakis, S. Das and M. Z. Bazant, *Joule*, 2021, **5**, 393–414.
38 X. Lu, M. Lagnoni, A. Bertei, S. Das, R. E. Owen, Q. Li, K. O'Regan, A. Wade, D. P. Finegan, E. Kendrick, M. Z. Bazant, D. J. L. Brett and P. R. Shearing, *Nat. Commun.*, 2023, **14**, 5127.
39 Z. Guo, J. Zhu, J. Feng and S. Du, *RSC Adv.*, 2015, **5**, 69514–69521.
40 X. Zhao, Y. Yin, Y. Hu and S.-Y. Choe, *J. Power Sources*, 2019, **418**, 61–73.
41 J. Li, B. Liu, S. Li, D. Hu, L. Wang and J. Xu, *J. Power Sources*, 2022, **521**, 230936.
42 X. Duan, B. Li, J. Li, X. Gao, L. Wang and J. Xu, *Adv. Energy Mater.*, 2023, **13**, 2203767.
43 M. Doyle, *J. Electrochem. Soc.*, 1993, **140**, 1526.
44 S. Santhanagopalan, Q. Guo, P. Ramadass and R. E. White, *J. Power Sources*, 2006, **156**, 620–628.
45 N. Legrand, B. Knosp, P. Desprez, F. Lapicque and S. Raël, *J. Power Sources*, 2014, **245**, 208–216.
46 A. Samba, N. Omar, H. Gualous, O. Capron, P. Van den Bossche and J. Van Mierlo, *Electrochim. Acta*, 2014, **147**, 319–329.
47 D. Ren, K. Smith, D. Guo, X. Han, X. Feng, L. Lu, M. Ouyang and J. Li, *J. Electrochem. Soc.*, 2018, **165**, A2167–A2178.

48 B. Liu, Y. Jia, C. Yuan, L. Wang, X. Gao, S. Yin and J. Xu, *Energy Storage Mater.*, 2020, **24**, 85–112.
49 J. R. Dahn, *Phys. Rev. B: Condens. Matter Mater. Phys.*, 1991, **44**, 9170–9177.
50 D. Fraggedakis, N. Nadkarni, T. Gao, T. Zhou, Y. Zhang, Y. Han, R. M. Stephens, Y. Shao-Horn and M. Z. Bazant, *Energy Environ. Sci.*, 2020, **13**, 2142–2152.
51 R. B. Smith, E. Khoo and M. Z. Bazant, *J. Phys. Chem. C*, 2017, **121**, 12505–12523.